

Multiphase microstructures via confined precipitation and dissolution of vessel phases: Example of austenite in martensitic steel

M. Belde, H. Springer,^{*} G. Inden and D. Raabe

Max-Planck-Institut für Eisenforschung GmbH, 40237 Düsseldorf, Germany

Received 2 July 2014; revised 14 November 2014; accepted 14 November 2014

Abstract—We present a novel method to locally control the constitution, morphology, dispersion and transformation behavior of multiphase materials. The approach is based on the targeted, site-specific formation and confined dissolution of precipitated carbides or intermetallic phases. These dispersoids act as “vessels” or “containers” for specific alloying elements forming controlled chemical gradients within the microstructure upon precipitation and subsequent (partial) dissolution at elevated temperatures. The basic processing sequence consists of three subsequent steps, namely: (i) matrix homogenization (conditioning step); (ii) nucleation and growth of the vessel phases (accumulation step); and (iii) (partial) vessel dissolution (dissolution step). The vessel phase method offers multiple pathways to create dispersed microstructures by the variation of plain thermomechanical parameters such as time, temperature and deformation. This local microstructure design enables us to optimize the mechanical property profiles of advanced structural materials such as high strength steels at comparatively lean alloy compositions. The approach is demonstrated on a 11.6Cr–0.32C (wt.%) steel, where by using $M_{23}C_6$ carbides as a vessel phase, Cr and C can be locally enriched so that the thus-lowered martensite start temperature allows the formation of a significant quantity of retained austenite (up to 14 vol.%) of fine dispersion and controlled morphology. The effects of processing parameters on the obtained microstructures are investigated, with a focus on the dissolution kinetics of the vessel carbides. The approach is referred to as vessel microstructure design.

© 2014 Acta Materialia Inc. Published by Elsevier Ltd. All rights reserved.

Keywords: High strength steels; Multiphase materials; Microstructure design; Carbides

1. Introduction

Advanced high strength steels derive their superior mechanical properties from the synergetic effects associated with precisely tuned multiphase microstructures, achieved by blending soft and ductile phases, such as ferrite or austenite, with hard and strong constituents, like martensite or bainite [1–3]. This is utilized for example in dual-phase (DP) steels, where finely dispersed martensite of 5–30 vol.% strengthens a ferritic matrix while retaining good formability [4–7], or in ultra-fine bainite, which consists of hard cementite aggregates within nanostructured bainitic ferrite [8,9]. For the design of ultra-high-strength steels, carbon-based (C) martensite and austenite are especially attractive microstructure constituents, as the former offers very high inherent strength, and the latter good ductility [10,11] coupled with additional work-hardening potential during deformation via the transformation induced plasticity (TRIP) mechanism [12,13].

Multiple alloying strategies and thermomechanical processing routes have been developed to achieve suitable microstructure blends, for example partially stabilizing

different phases chemically against quenching or transformation by introducing phase-specific alloying elements. As utilized in welds of duplex (ferritic/austenitic) steels [14], for example, the type of phases formed, as a function of the respective alloy concentrations, can be predicted using Schaeffler-type diagrams [15]. While this approach typically relies on rather high bulk alloying contents, as for example in stainless steels, the much leaner DP and TRIP-assisted steels widely used in automotive applications are produced by annealing in a two-phase (austenitic/ferritic) region, before cooling to room temperature following different time–temperature profiles [16,17]. This approach exploits the partitioning of alloying elements taking place during this intercritical holding, especially that of C, which leads to pronounced deviations in composition of the individual phases from the bulk values. This effect is aimed at tuning the local phase stabilities [18,19]. More complex processing, such as quenching – to above or below the martensite start (M_s) temperature – coupled with subsequent tempering, may lead to precipitation and additional phase transformations, for instance yielding retained or reverted nanoscaled austenite in a tempered martensitic matrix [10,11,20–23].

All the aforementioned processes can be very effective in controlling the type and fractions of the blended phases. However, at least equally important for the

^{*} Corresponding author; e-mail: h.springer@mpie.de

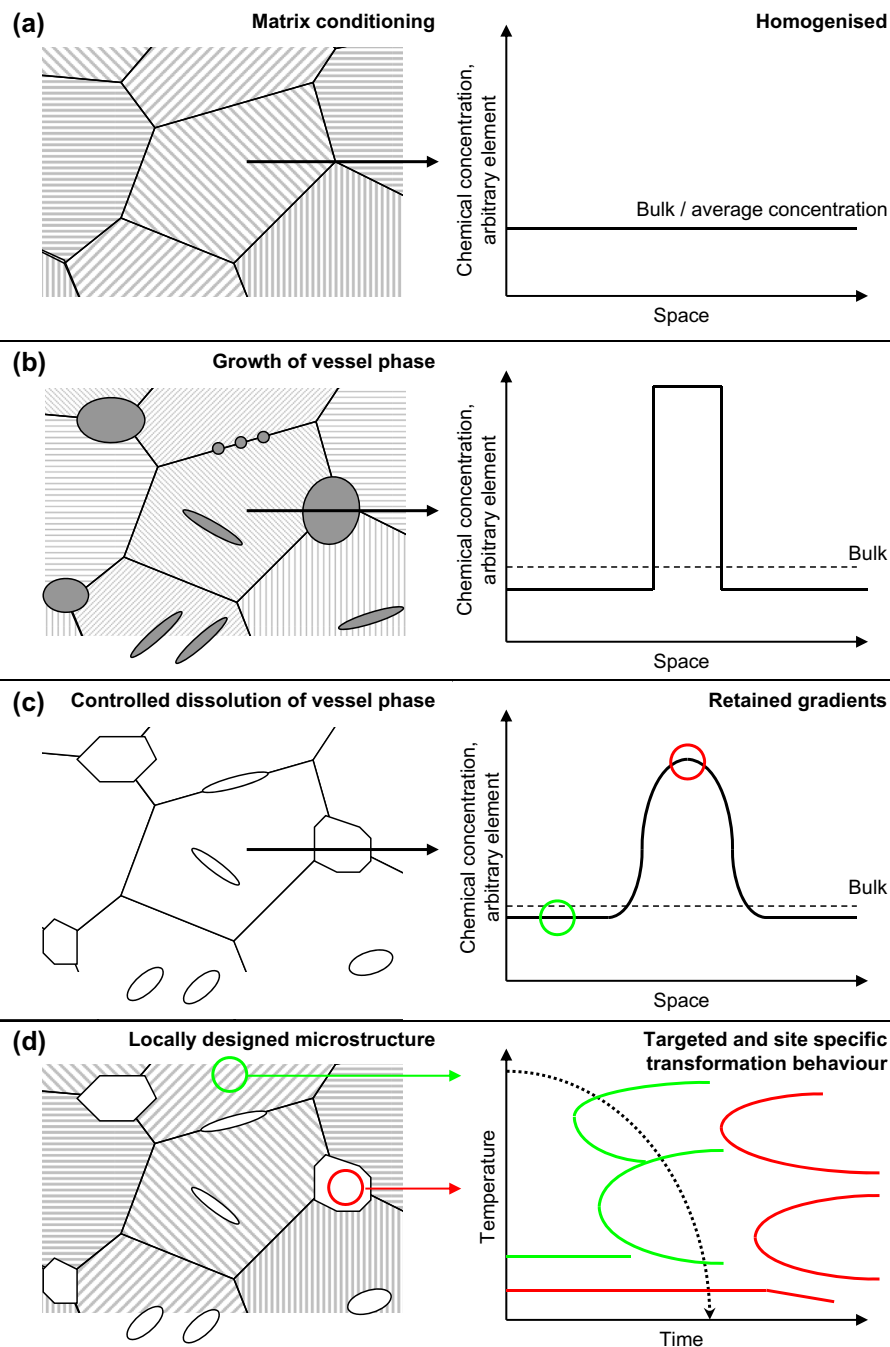


Fig. 1. Sketch illustrating the proposed vessel microstructure design approach; (a) step 1, matrix conditioning, exemplified by homogenization; (b) step 2, accumulation of alloying elements in “vessel” precipitates nucleating under conditions imposed by the matrix conditioning; (c) step 3, dissolution of the vessel phase leads to chemical gradients, creating a chemically inhomogeneous matrix, constituting local alloying; (d) result: local changes in composition locally modify phase stability and morphology.

mechanical properties, especially ductility and toughness, is the local microstructure build-up in terms of dispersion, morphology and size of the constituents. Examples are the size and morphology of martensite islands as important factors governing crack initiation in DP steels [4,24] or the size dependence of austenite stability against its transformation in ultra-high-strength steels [19,25,26]. To further optimize such complex alloys in this regard the established processing and alloying routes are limited, as they offer only restricted and indirect control over the site-specific nucleation and stability

conditions of a given phase which may be desired for the local mechanical response. It thus becomes clear that in order to more effectively design innovative structural materials, it is of great interest to be able to control not only which types of phases are formed, but also simultaneously design their morphology, dispersion and stability.

The local phase stability and transformation behavior are determined by the local chemical concentration. As sketched in Fig. 1a, bulk alloying defines phase composition and hence stability, only in case of ideal

homogenization. The novel design approach presented here is based on using particles or precipitates formed during aging. They are, however, not used to directly alter the mechanical properties via the Orowan mechanism, but as temporary reservoirs for the site-specific accumulation and release of alloying elements (Fig. 1b). When such a temporary precipitate phase, hereafter referred to as a “vessel phase”, is subsequently (partially) dissolved at higher temperatures, the chemical elements dissolving from it form local chemical gradients in the surrounding matrix. The persistence of these gradients depends on the vessel phase stability, temperature, time and dissolving elements [27]. Hence, if the alloying and annealing conditions are chosen appropriately, finely dispersed chemical gradients are formed, inheriting both location and morphology of the dissolved vessel phase (Fig. 1c). Upon cooling to room temperature, this chemically inhomogeneous microstructure now exhibits locally differing time–temperature–transformation profiles (Fig. 1d), enabling “self-organized” microstructure design. This novel sequence of processing allows for controlling the type of vessel phase via an adequate choice of alloying elements and aging regime, and thus which elements are accumulated for a specific desired effect (e.g. phase type and stability). Further, the method predetermines the geometry and, most importantly, the location and dispersion of such chemical concentration profiles by adjusting nucleation and growth conditions for the vessel within the matrix phase. The approach of using targeted and site-specific vessel particle growth and dissolution to induce local chemical gradients thus offers a wide range of tuneable parameters to achieve tailored microstructure blends.

The following requirements apply for a vessel phase to be effective: (i) it should have a significantly different chemical composition from the bulk alloy; (ii) it should possess a limited temperature range of thermodynamic stability so that it can dissolve upon heat treatment; and (iii) it should be capable of assuming different morphologies, dependent on aging, alloying and interface energy. Consequently, alloy carbides are an ideal choice in the case of steels, as their composition and stability are well understood and can be calculated by CALPHAD and quantum mechanical methods [28–31]. Furthermore, their nucleation, growth and dissolution mechanisms [32–35] have been subject to extensive research, due to their widespread application, for instance in creep-resistant steels [36,37]. Carbides of the type $M_{23}C_6$ are especially promising, as they offer a combination of comparatively rapid growth, limited stability and high alloy content, most notably of chromium (Cr). Cr significantly reduces the M_s temperature, but – as a ferrite stabilizer – typically cannot be enriched in or partitioned to austenite [38]. Furthermore, Cr is relatively cost-effective, confers both strengthening and corrosion resistance and is reported to reduce the activity and diffusion kinetics of the accompanying C [22,39,40]. Consequently, by way of locally varied combinations of Cr and C, a variety of alternative kinetic pathways is available for tailoring retained austenite in martensitic steel.

2. Objective

The goal of this work is to demonstrate how bulk multiphase microstructures can be locally tailored by the confined precipitation and dissolution of vessel phases. This novel design method enables creating self-organized local

chemical gradients, thus opening novel pathways for tuning dispersed microstructures with defined phase stability towards optimized mechanical properties of structural materials. The approach is validated on the example of targeted growth and dissolution of $M_{23}C_6$ carbides, which were used to obtain locally controlled Cr- and C-enriched areas for blending metastable retained austenite within a high strength martensitic matrix.

3. Experimental

3.1. Materials production and processing

The Fe–Cr–C alloy used in this study was produced by vacuum induction melting (1 kg charge weight), cast into a copper mould with the internal dimensions of $25 \times 60 \text{ mm}^2$, subsequently rolled at $1100 \text{ }^\circ\text{C}$ from 25 to 4.8 mm thickness and air-cooled to room temperature. After this pre-processing, its composition according to wet chemical analysis was Fe–11.6Cr–0.323C (wt.%), with aluminum, silicon, manganese, nickel and nitrogen all below 0.008 wt.%. From the as-rolled billet, bulk samples of $60 \times 20 \times 4.8 \text{ mm}^3$ were cut by spark erosion. Prior to microstructure analysis and dilatometry, the sheets were ground to 4 mm thickness to remove oxide scales and decarburized regions, and $4 \times 4 \times 10 \text{ mm}^3$ samples were prepared by spark erosion.

The vessel phase approach proposed in this work was realized in the chosen example by three subsequent heat treatments, each step exerting influence on both the vessel and matrix properties (Fig. 2a). The first step, referred to as conditioning, is performed to achieve thorough homogenization and attain supersaturated martensite. Bulk samples were held at $1150 \text{ }^\circ\text{C}$ for 2 h in a horizontal glass-tube furnace under an argon atmosphere of $1.2 \times 10^5 \text{ Pa}$ and subsequently quenched in oil to room temperature. The second step, termed accumulation, comprises nucleation and growth of carbides. For this step, bulk samples were held at $750 \text{ }^\circ\text{C}$ for 47 h under argon, followed by oil-quenching. The last step, termed dissolution, aims at dissolving the vessel carbides while locally retaining the associated Cr accumulation through rapid heating, in order to obtain inhomogeneous austenite. These transient heat treatments were performed using a Baehr Dil805 dilatometer, equipped with induction heating of 32 kHz, under a protective hydrogen atmosphere of 10^3 Pa . Heating and cooling rates were set to be $200 \text{ }^\circ\text{C s}^{-1}$ with holding times of 1–90 s at temperatures of 850–1350 $^\circ\text{C}$. Quenching to room temperature was carried out using hydrogen gas.

The choice of processing parameters was guided by CALPHAD predictions, using Thermo-Calc 3.0.1 and DICTRA 27.01 software packages [41], in conjunction with databases TCFE7 and mobfe2. The first two processing steps (conditioning and accumulation) represent equilibrium processes and were therefore evaluated using Thermo-Calc. Fig. 2b shows the predicted phase volume fractions vs. temperature. Homogenization was performed well above the austenitization temperature to ensure complete carbide dissolution and optimum equalization of the Cr concentration across the specimen. The accumulation temperature was chosen as high as possible, while still safely exploiting the higher Cr diffusivity of the ferrite lattice and avoiding phases other than ferrite and $M_{23}C_6$.

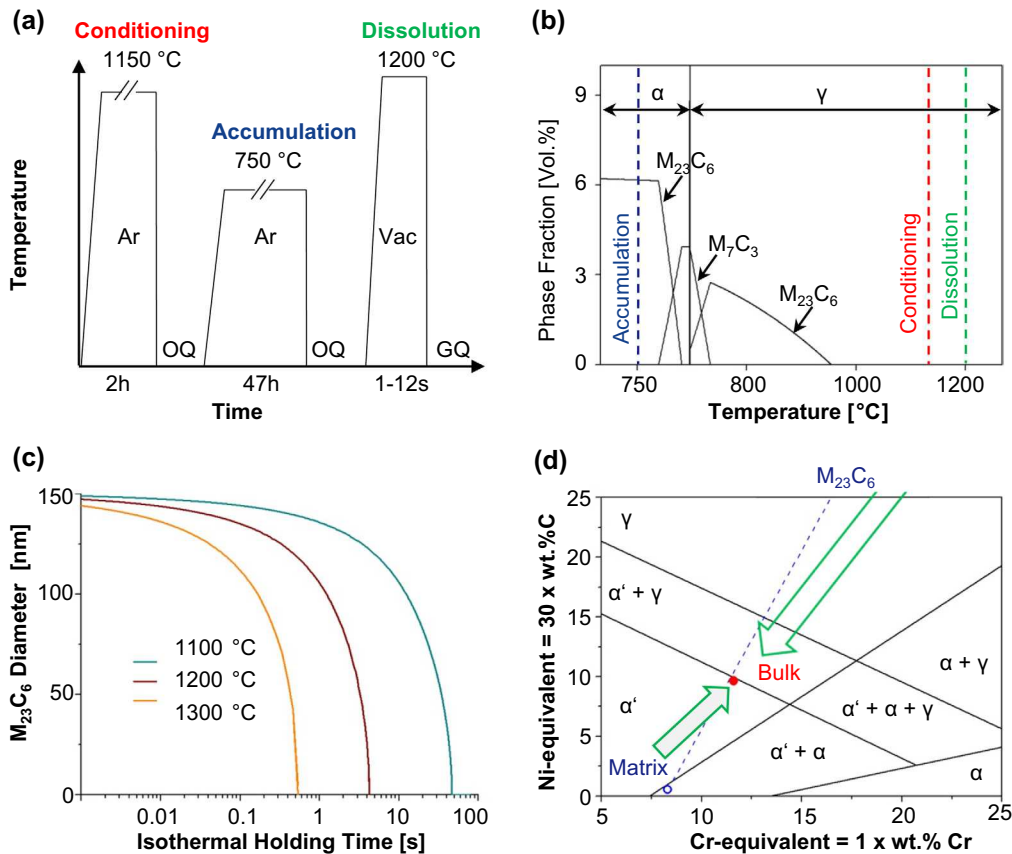


Fig. 2. (a) Exemplified processing steps in a time–temperature overview; (b) Thermo-Calc phase diagram for the alloy of this study Fe–11.6Cr–0.32C (wt.%); (c) DICTRA calculation of the isothermal carbide dissolution at different temperatures; (d) Schaeffler diagram predicting as-quenched microstructures [15]. Conditioned bulk state and accumulated matrix- $M_{23}C_6$ range (by Thermo-Calc) are indicated for reference. The dissolution process is indicated by the gray arrows.

Predicting the third and last processing step, namely dissolution, requires some kinetic considerations. The boundary conditions are set by the aim to dissolve the vessel phase without homogenizing the chemical composition throughout the matrix, i.e. diffusion should remain confined to preserve the desired chemical gradients. Thus DICTRA calculations were made, reproducing simplified carbide morphologies with equilibrium starting composition, present after accumulation. Fig. 2c shows calculated dissolution kinetics of $M_{23}C_6$ in homogeneous austenite. This simulation guided the final heat treatment step. A fixed carbide diameter is predicted to decrease by an order of magnitude faster per 100 °C temperature increase. The assumptions made in these calculations and the associated implications are discussed in more detail in Section 5.2. It should be mentioned that the vessel phase approach can in principle also be applied in the form of incomplete particle dissolution, for instance when aiming at designing core–shell structures.

Empirical microstructure estimates for the three processing steps were also derived as trends from the Schaeffler diagram [15], as shown in Fig. 2d. It should be noted though that these latter estimates are based on empirical equations, determined for a specific alloying concentration range, and may thus have limited transferability to the compositions used here. The homogenized and quenched bulk state (conditioning) is predicted to be fully martensitic, but close to the austenite border, offering excellent starting

conditions for the desired formation of dispersed, retained austenite. For the second processing step (accumulation) the ferrite and a tie-line to the $M_{23}C_6$ composition (not covered in the diagram), as calculated by Thermo-Calc, are shown. In the third step (dissolution), elemental pile-ups of Cr and C have to be conserved by quenching as the microstructure converges back towards a chemically homogeneous bulk state.

3.2. Characterization

Sections perpendicular to the transverse direction (TD) and rolling direction (RD) were prepared for microstructure observation by standard mechanical grinding and polishing techniques. Microstructure analysis was performed using field emission scanning electron microscopy (SEM; ZEISS FIB 1540 XB and JEOL JSM 6500) equipped with energy-dispersive X-ray analysis (EDAX), energy-dispersive X-ray spectroscopy (EDS) and electron backscattered diffraction (EBSD) systems (TSL OIM software, version 6.2). Transmission electron microscopy (TEM) samples were produced by cutting 3 mm disks from cylindrical dilatometry samples, grinding them to 100 μm thickness, followed by double jet electropolishing with A8 electrolyte. Phase fractions were determined by X-ray diffraction (XRD; Seifert ID003 with an energy dispersive Meteor0D point detector) with Co K_{α} radiation at 40 kV/30 mA, followed by Rietveld analysis using MAUD software [42].

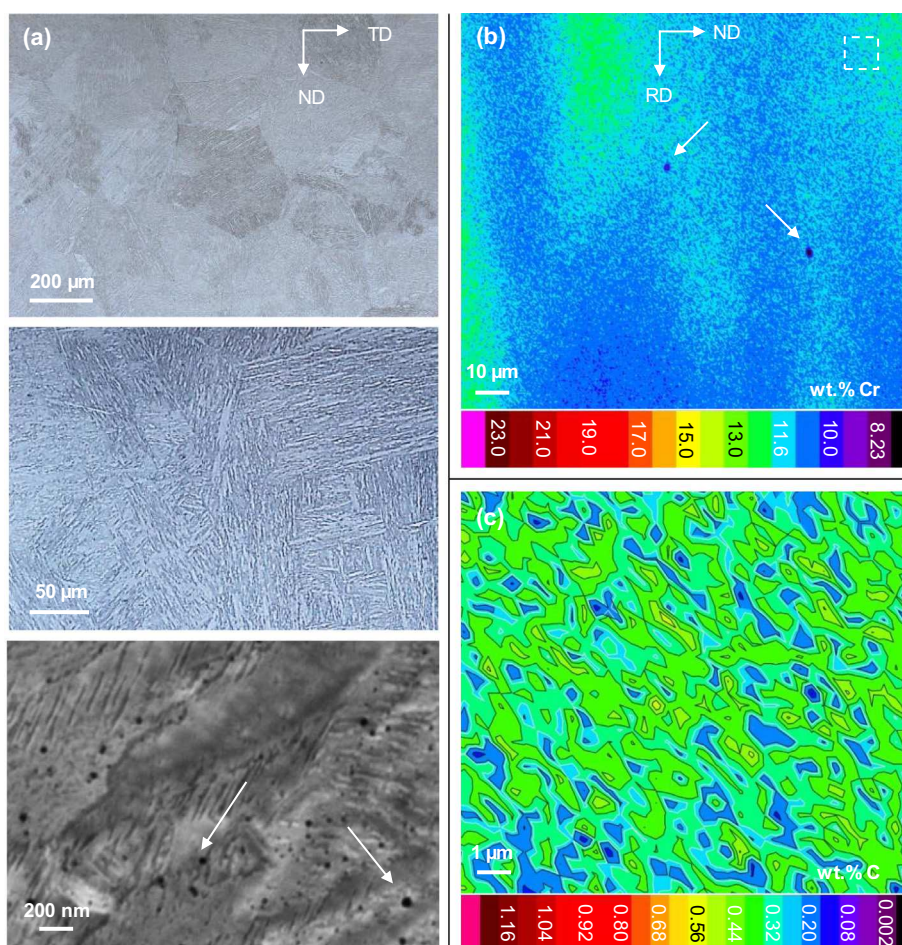


Fig. 3. Analysis of the as-conditioned microstructure (1150 °C, 2 h, oil-quenched), (a) light-optical (top, middle) and SEM micrographs (bottom), arrows denote etching artefacts; (b) color-coded EPMA mapping of the Cr distribution, arrows denote pores; (c) corresponding mapping for C distribution of the area marked by the dashed rectangle in (b). (For interpretation of the references to color in this figure legend, the reader is referred to the web version of this article.)

Chemical gradients were examined by electron probe micro-analysis (EPMA; JEOL JXA-8100, heat emission, 12 kV) area mappings, using a pure iron (Fe) standard and a step size of 0.3 μm . These were augmented by TEM (Philips CM20, 200 kV, EDAX DX Prime EDS) and Auger spectroscopy (JEOL JAMP-9500F) operated at 25 kV, with an electrostatic hemispherical analyser and implemented software. Rockwell C hardness was tested on the examined cross-sections employing a Wolpert DIA Testor 2RC. Tensile testing was conducted using an Instron 8511 testing machine, with an initial strain rate of 10^{-3} s^{-1} on cylindrical specimens, suitable for dilatometer treatments, with a gauge length of 2 mm.

4. Results

4.1. Conditioning of the microstructure and accumulation of chemical gradients

Light optical microscopic observation after the homogenization treatment (2 h at 1150 °C, oil quenching) showed a fully martensitic microstructure free of coarse carbides, Fig. 3a, with a prior austenite grain size of $\sim 350 \mu\text{m}$ and a hardness of 58.7 HRC. SEM investigations at higher magnification (Fig. 3a, bottom) confirmed the absence of

fine carbides, which may form by self-tempering during quenching [43]. This effect is unlikely though, owing to the comparatively low M_s temperature (284 °C as measured by dilatometry; 285 °C according to empirical calculations [38]). The small dark features (white arrows in Fig. 3a, bottom) most probably constitute etching artefacts. The targeted chemical homogeneity of the sample in conditioned state was examined by EPMA area mapping of Cr and C, as shown in Fig. 3b and c. The color legends are scaled to be consistent with those used to map the later processing stages. The maps show only small fluctuations at the micrometric scale; in the case of Cr, residual traces of casting segregations can be observed.

Tempering for 47 h at 750 °C of the above described homogenized microstructure (accumulation step) resulted in the transformation of martensite into ferrite and the precipitation of carbides, to serve as the vessel phase. SEM micrograph analysis (Fig. 4a) in conjunction with ImageJ software [44] revealed a mean carbide diameter of 0.3 μm . Most carbides were elongated along the ferrite grain boundaries (former martensite lath boundaries) with an average aspect ratio of 0.47. EBSD spot analysis proved the carbides to be solely of the type $M_{23}C_6$ (Fig. 4a, inset), in accordance with Thermo-Calc predictions (Fig. 2b). The chemical gradients accumulated by tempering are shown in the color-coded EPMA maps of Fig. 4b. The

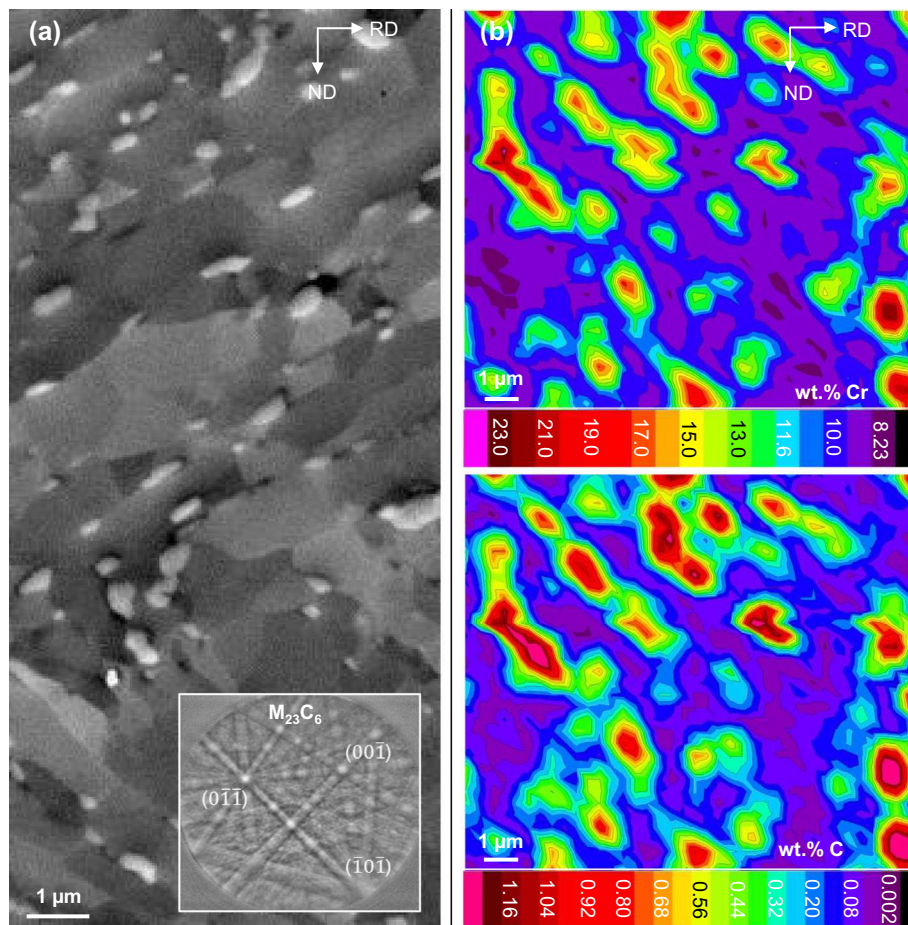


Fig. 4. Analysis of the conditioned and accumulated microstructure (1150 °C, 2 h, oil quenched and tempered 750 °C, 47 h): (a) SEM micrograph and indexed EBSD pattern of the M₂₃C₆ carbides; (b) color-coded EPMA mapping showing accumulation of Cr (top) and C (bottom). (For interpretation of the references to color in this figure legend, the reader is referred to the web version of this article.)

Table 1. Retained austenite fractions, as measured by XRD, obtained for different holding times and temperatures.

Holding time [s]	Austenite fraction [vol.%]		
	1100 °C	1200 °C	1300 °C
1	2.7	8.7	12.3
3	5.5	14.1	7.1
6	5.3	3.1	4.0
9	5.1	4.1	1.9
12	5.9	0.5	0.9
30	6.0		
60	2.5		
90	0.7		

ferrite–carbide microstructure is reproduced in locally concerted gradients of Cr and C. Enriched and depleted zones are clearly visible. With regard to the resolution of the method and the feature sizes, up to 23 wt.% Cr and 1.2 wt.% C were measured within the carbides, while the Cr and C contents of the ferritic matrix were consequently lowered, from 11.6 to ~8–10 wt.%, and from 0.323 to 0.002–0.140 wt.%, respectively.

4.2. Dissolution of the carbide vessels

High temperature annealing was performed as the final processing step to dissolve the carbides formed during

tempering, but in sufficiently short times to retain the chemical gradients accumulated by the carbide vessels (dissolution step). The viable processing window for obtaining retained austenite reached from 950 to 1350 °C. Table 1 gives an impression of the respective austenite retention kinetics for holding at selected temperatures as determined by XRD. Lower temperatures give a wider range of annealing times but limited austenite fraction, while higher temperatures reverse this relationship. The highest austenite fraction was obtained at intermediate temperatures, with 14.1 vol.% for 3 s holding at 1200 °C. The focus of the investigations was, therefore, on short annealing times at this temperature, in order to track the dissolution and diffusion processes and their relation to the respective phase transformation phenomena taking place in the chosen model alloy system. Fig. 5 compiles results obtained from annealing at 1200 °C for 1 s. The hardness is at 50.8 HRC, lower than after conventional homogenization annealing at 1150 °C for 2 h and water quenching (58.7 HRC). Complete austenitization of the ferritic matrix was reached at 942 °C after 0.3 s according to dilatometry. As shown in the color-coded EBSD phase map of Fig. 5a, 9.6 vol.% of austenite (green) could be detected within the martensitic matrix (red). The martensite inherited the fine and globular morphology of ferrite in the as-tempered sample (Fig. 4), with a mean grain diameter of ~1.4 μm, as given by the OIM software. The austenite grain size varies from ~0.1 to 2 μm (mean 0.5 μm), with an average

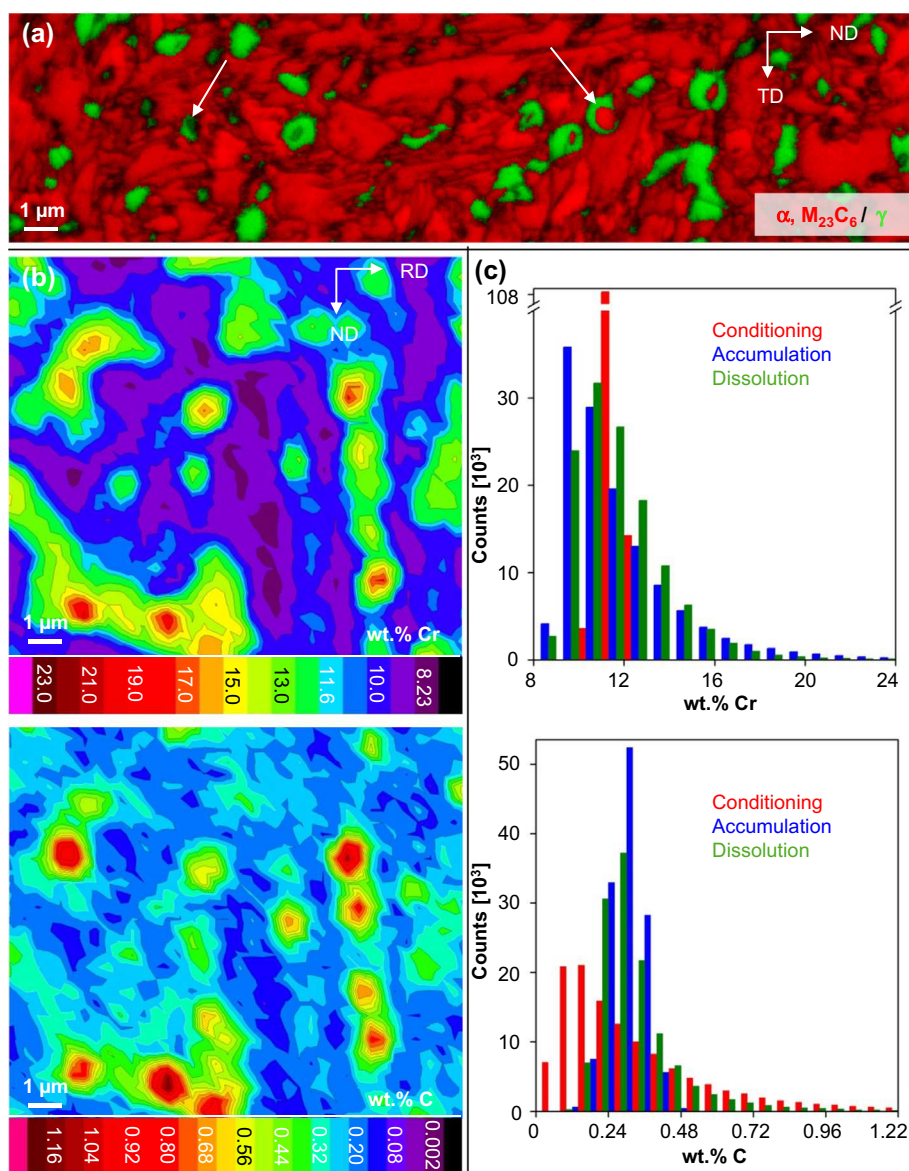


Fig. 5. Analysis of the conditioned and accumulated microstructure after dissolution (1200 °C, 1 s, gas-quenched): (a) color-coded EBSD phase map with image quality data superimposed in gray scale, arrows denote austenite shells surrounding carbides; (b) color-coded EPMA maps of Cr (top) and C (bottom); (c) histograms of the EPMA data for all three processing stages. (For interpretation of the references to color in this figure legend, the reader is referred to the web version of this article.)

aspect ratio of 0.49, matching the original shape of the carbide vessel phase. Enveloped within few austenite grains, some residual carbides can be observed (indicated by white arrows in Fig. 5a, mis-indexed as α -Fe) which were not fully dissolved at this very short annealing time. Carbides can, however, be clearly distinguished from ferrite in terms of shape and image quality, which is superimposed on the micrograph in gray scale. The austenite fraction was measured by XRD to be 8.7 vol.% in the longitudinal section, which agrees well with the EBSD results. The bulk M_S temperature was determined as 360 °C, a significant increase compared to the as-homogenized samples (284 °C).

The obtained chemical gradients are shown as color-coded EPMA mappings in Fig. 5b. Compared to the accumulation stage (Fig. 4b), appreciably fewer joint maxima of Cr and C levels are present. Additionally, the region of impingement between maxima has increased for both elements, thus surpassing the observed austenite grains in

dimension, but agreeing reasonably well with the EBSD findings (Fig. 5a). The evolution of chemical gradients throughout the entire vessel processing cycle (homogenization, accumulation, dissolution) is summarized in histograms for both alloying elements in Fig. 5c, with bin sizes identical to the scaling of the mappings shown previously. It can be clearly seen that after dissolution the C levels are again close to those during homogenization, whereas the Cr gradients are more similar to the accumulated state. The respective decrease in carbide volume fraction upon dissolution is evident from the respectively decreased number and levels of peak populations in Cr and C.

High resolution investigation results for the same partial dissolution condition described above (1200 °C, 1 s) are summarized in Fig. 6. For a direct spatial comparison of chemistry with crystallography, a combined EBSD–EDS mapping was carried out (Fig. 6a). While the resolution is limited and contamination inhibits measuring the C

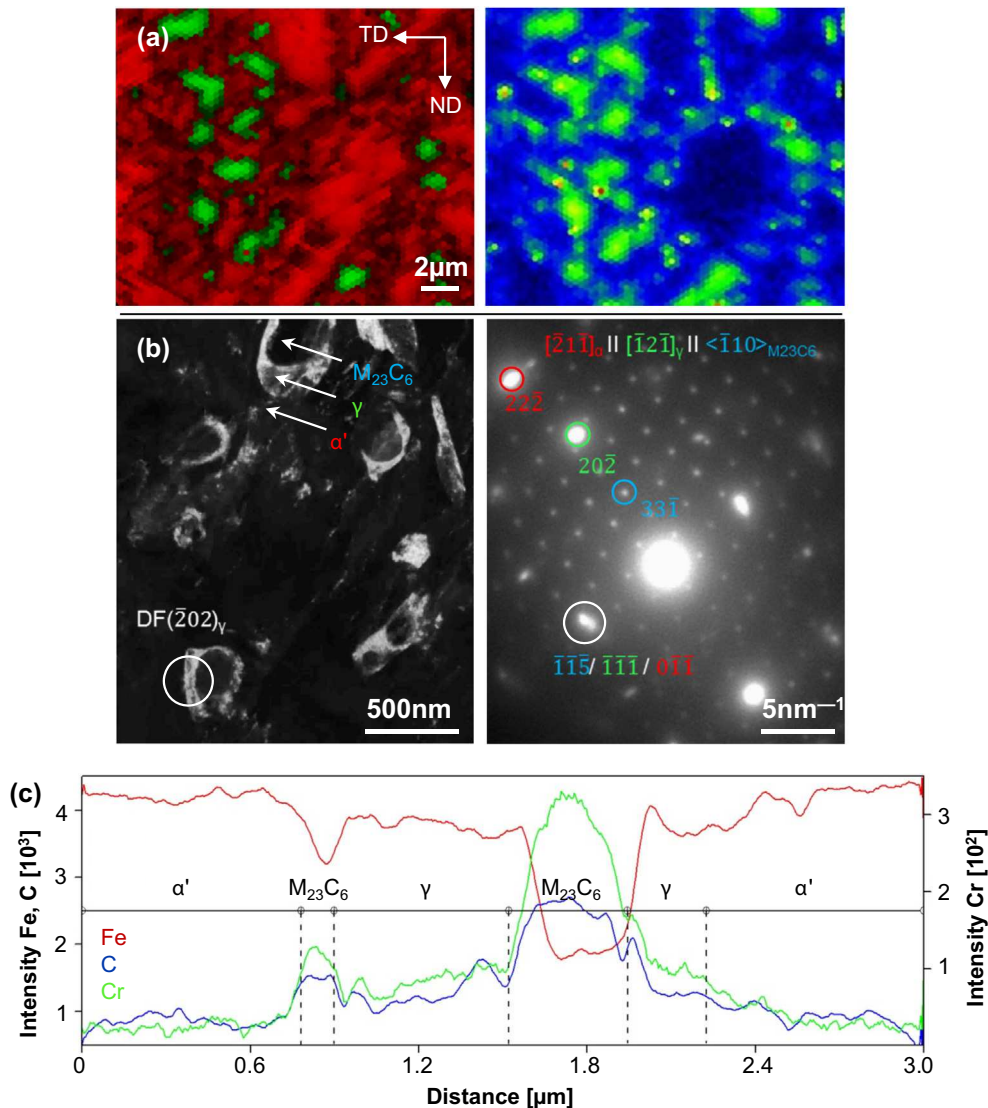


Fig. 6. High resolution characterization of the conditioned and accumulated microstructure after dissolution (1200 °C, 1 s, gas-quenched): (a) correlative EBSD (left) and EDS mapping correlating retained austenite (green) and Cr enrichment (1000–3000 counts, blue to red); (b) TEM dark field overview showing austenite shells surrounding partially dissolved carbides (left), with selected area diffraction of the circled area (right) showing a K–S relationship between martensite and austenite; (c) qualitative Auger spectroscopy line-scan result across partially dissolved carbides. (For interpretation of the references to color in this figure legend, the reader is referred to the web version of this article.)

concentration reliably, a good agreement between Cr-enriched areas and austenite can be observed. As found by the overview EPMA mappings in Fig. 5b, the size of the measured Cr-enriched zones often exceed in size that of the carbide–austenite aggregates, illustrating a necessary critical threshold value in Cr content for austenite stabilization. TEM analysis gives a more detailed picture of the three-phase microstructure, exemplified by the dark field micrograph in Fig. 6b, showing austenite surrounding non-dissolved carbides in support of the preceding EBSD findings. The (−202)-oriented austenite grains fulfil shared Bragg conditions: the encased carbides appear to be close to their initial mean size and their austenite shells are correspondingly thin. Crystallographic investigation and validation (exemplified in Fig. 6b) also detected a Kurdjumov–Sachs (K–S) orientation relationship between austenite and martensite. TEM EDS at the same time provided chemical composition at high spatial resolution. M₂₃C₆ carbides

contained 65.8 ± 3.0 wt.% Cr, matching the equilibrium concentration of 65.5 wt.%, given by Thermo-Calc for the accumulation condition. Austenite was determined to contain 20.8 ± 4.0 wt.% Cr by isolated spot measurements. The Cr content of the martensite was lowered compared to its original bulk mean value to a homogeneous level of 9.9 ± 0.5 wt.%, which is in fair agreement with the EPMA data.

In order to obtain a better insight into the transport phenomena taking place within this transient state, Auger spectroscopy was performed on a large carbide–austenite aggregate (Fig. 6c). The sampled depth was estimated as 3.0 nm for Cr and 2.4 nm for C, by using a three mean free path (3λ) approximation for 90% intensity [45]. An EBSD measurement of the area, before and after the Auger scan, enabled relating chemical and crystallographic information, as well as ruling out the influence of milling. Spot measurements indicated compositions of 53.3, 22.1 and

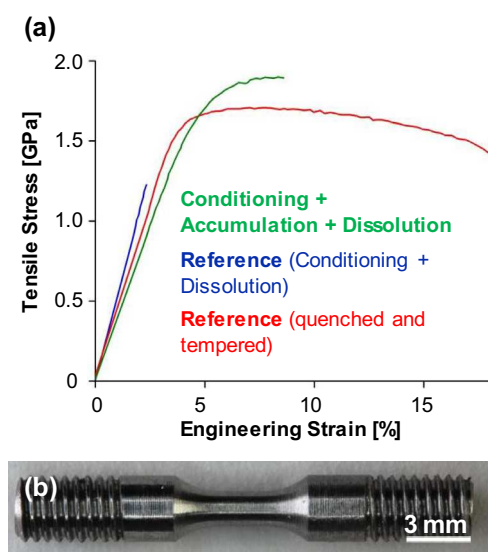


Fig. 7. (a) Engineering stress–strain curve (green) of the conditioned and accumulated microstructure after dissolution (1200 °C, 1 s, gas-quenched) together with two reference conditions: identical treatment but without accumulation (blue curve), conditioning and subsequent annealing at 400 °C for 30 min (quenched and tempered, red curve); (b) tensile testing specimen for dilatometer heat treatments. (For interpretation of the references to color in this figure legend, the reader is referred to the web version of this article.)

10.5 wt.% Cr for the carbide, austenite and martensite, respectively, consistent with the TEM EDS data. Due to its diffusion to the surface in the sampled volume as well as beam contamination, C concentrations could not be quantified, but significant enrichment in austenite was indicated. The compositions are shown for each element as a signal minus background value, normalized by background in Fig. 6c. This qualitative Auger line scan shows a case of impinging gradients, wherein a small carbide is dissolving next to a larger one, resulting in the enclosed austenite being stabilized and retained to room temperature. In this intermediate area Cr and C show a similar slope of intensities growing towards the larger carbide. The right flank of the larger carbide shows a steep gradient, unaltered by impingement, down towards the martensite, whereas to the left of the small carbide, both Cr and C decrease rapidly and concurrently in the martensite. The martensite itself appears invariant at both scan edges, indicating a stable matrix composition. On the rightmost flank, both gradients show a pronounced slope within the austenite, leveling off, with C exhibiting a slightly steeper gradient. No striking discontinuity in concentration profiles marks the austenite/martensite interface. Above a critical enrichment of both Cr and C, austenite is retained as a consequence of this chemical stabilization.

4.3. Mechanical properties

The conditioned material (homogenized and oil-quenched) has an average hardness of 58.7 HRC, which was lowered to 174 HV1 by the subsequent accumulation treatment (tempering). After the final processing step, i.e. dissolution of the vessel carbides (at 1200 °C for 1 s), a value of 50.8 HRC was obtained. For comparison, two reference treatments were applied to the Fe–Cr–C model alloy:

- (i) Direct dissolution annealing (1200 °C for 1 s) after conditioning without intermediate accumulation. In accordance with Schaeffler-type predictions [15], this treatment resulted in a fully martensitic microstructure and a hardness of 50.7 HRC.
- (ii) Tempering at 400 °C for 30 min after conditioning, aimed at stabilizing reverted austenite within a tempered martensitic matrix [10,11]. Thus, up to 8.4 vol.% (XRD) of reverted austenite could be obtained at a hardness of 46.7 HRC.

Tensile testing results (Fig. 7) show that the presented processing approach resulted in a very high strength of 1.9 GPa and a total elongation – without any indications of necking – of ~8% strain (green curve in Fig. 7a). At almost identical hardness, the non-accumulated reference treatment (blue curve in Fig. 7a) resulted in brittle failure at low strain during the elastic regime. The conditioned and tempered reference, on the other hand (red curve in Fig. 7a), showed much higher ductility, achieving 18% total elongation and a lower tensile strength of 1.7 GPa, as can be expected from its lower hardness. Remarkably, uniform elongations are comparable between the materials in tempered (red) and quenched (green) states, as are the austenite fractions (8.7 vol.% retained vs. 8.4 vol.% reverted) prior to deformation. Varying the time and temperature during the dissolution step of the proposed approach significantly altered not only the austenite fractions (Table 1) but also the corresponding mechanical properties of the material: specimens with a higher austenite content (1300 °C for 1 s, 12.3 vol.% austenite) exhibited similar hardness (52.7 HRC) and brittle failure at 1.2 GPa without plastic deformation during tensile testing. A reduced austenite content (1100 °C for 1 s, 2.7 vol.% austenite) yielded lower hardness (46.8 HRC) and significant ductility (12% total elongation) during tensile testing, albeit at lower ultimate tensile strength (1.6 GPa) than for the 1200 °C sample (Fig. 7a). It has to be noted that the non-standardized sample geometries (Fig. 7b), chosen here to comply with dilatometer processing, may affect the respective tensile properties. Also, small sample sizes and the indirect strain measurements may have led to overestimated elongations.

4.4. Effects of different processing variations

In addition to controlling the austenite volume fraction by dissolution, changes to preliminary processing were introduced to adjust vessel alignment, shape and position. SEM micrographs shown in Fig. 8 illustrate the results of two alternative routes of preparing gradients for dissolution. Firstly, preferential alignment of the $M_{23}C_6$ precipitations was achieved, Fig. 8a, by omitting homogenization treatment and starting with the accumulation step (750 °C, 47 h) after hot rolling (at 1100 °C) and air cooling. Casting segregations (traces in Fig. 3b) were thus retained and subsequently enhanced by rolling, constituting pre-accumulated Cr gradients in the air-cooled martensite. The resulting banded structure thus resembles that observed in industrially produced steels [11]. Carbides preferentially precipitated along the RD and reached slightly larger diameters. When subjected to the same previously examined dissolution treatment (1200 °C, 1 s), noticeably banded austenite resulted. The increase in austenite fraction to 12.7 vol.% according to XRD, compared to the case of homogeneous dispersion (Section 4.2), may be related to overlapping dissolution

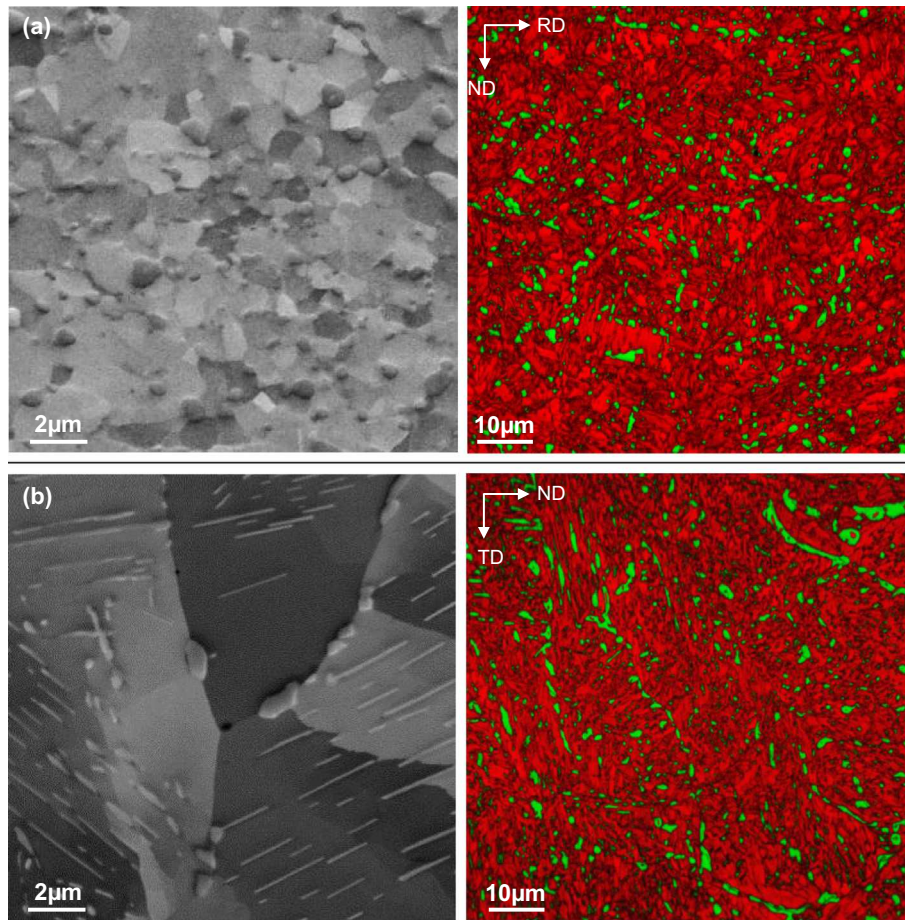


Fig. 8. Effects of alternative conditioning routes on the accumulated microstructure (SEM micrographs, left) and in turn the austenite morphology after subsequent dissolution (EBSD phase maps, right): (a) slightly banded microstructure achieved by direct accumulating from the hot-rolled condition without prior homogenization; (b) lamellar and grain boundary carbides/austenite achieved by discontinuous precipitation via furnace cooling from homogenization to accumulation (without intermediate quenching).

fields of adjacent carbides. A second attempt was aimed at changing vessel shape and location by linking conditioning (1150 °C, 2 h, furnace cooling) with an extended accumulation period (750 °C, 70 h). This resulted in discontinuous precipitation of lamellar carbides during $\gamma \rightarrow \alpha$ phase transformation as well as pronounced austenite grain boundary precipitation (Fig. 8b). Since the carbides are expected to form within a less diffusive austenite/ferrite matrix, the time for accumulation was consequently extended to compensate for this effect. The resulting 11.2 vol.% of austenite observed after dissolution (1200 °C, 1 s) accordingly decorate the prior austenite grain boundaries and also present elongated shapes inside those grains, although spheroidization hampered the strict inheritance of the originally lamellar carbide morphology.

5. Discussion

5.1. Microstructure evolution during processing and resulting mechanical properties

Following the novel vessel processing approach proposed in this work, self-organized chemical gradients were induced within a Fe–11.6Cr–0.32C alloy by the targeted growth and dissolution of $M_{23}C_6$ carbides, acting as vessels

phases to locally accumulate Cr and C (Figs. 5b and c). Due to the locally lowered M_s temperature of the Cr- and C-enriched areas, up to 14.1 vol.% of retained austenite could thus be incorporated within a non-tempered martensitic matrix. This is remarkable as the substantial formation of retained austenite is otherwise impossible for this lean chemical composition, and thus demonstrates how the presented approach opens novel pathways for the development of cost-efficient structural materials with complex phases. Crucially, the vessel concept also offers the possibility to control the size, morphology and location of the austenite within the microstructure (Figs. 5a and 8).

The coarse prior austenite grain size incurred during the first processing step (conditioning) ensures that most carbides nucleate and grow at martensite lath boundaries, i.e. inside the original austenite grain [46], rather than at prior austenite grain boundaries [47]. Besides promoting nucleation of precipitates, martensite also offers increased diffusivity of substitutional atoms [48] during the subsequent accumulation step. The accumulation state microstructure after the reference processing (Fig. 2a) resembles that of a tempered martensitic steel, as used for example in power plants, in an over-aged condition [49], consisting of rather coarse carbides in recrystallized ferrite (Fig. 4a). The prior martensitic lath structure is still apparent in the

form of aligned carbide strings, which are assumed to have formed in the sequence of $M_3C \rightarrow M_7C_3 \rightarrow M_{23}C_6$, with successively increasing Cr content in the carbides [22,43]. Assuming that the carbide volume fraction is given by the equilibrium value (6.16 vol.%, Fig. 2b) according to Thermo-Calc, the resulting matrix composition amounts to 8.32 wt.% Cr and 0.002 wt.% C, which is in good agreement with the EPMA results (Fig. 4b). The accumulation microstructure can hence be considered to follow approximate thermodynamic equilibrium conditions, which is also confirmed by the TEM EDS results obtained for the carbides in dissolution state (see Section 4.2).

The final processing step of dissolution resulted in a homogeneously dispersed microstructure consisting of martensite, globular and evenly distributed (in case of prior accumulation) austenite and – depending on the annealing parameters – non-dissolved carbides (Fig. 5a). With the exception of the areas directly adjacent to the (dissolved) carbides, the martensitic matrix can be considered as chemically homogeneous. This is supported by the TEM EDS and EPMA data (Section 4.2). The martensite is less coarse and of a more globular morphology than after homogenization (Fig. 3a). This refinement of the martensite matrix is expected to stem from austenitization of the fine-grained accumulated starting condition [50]. Austenite is reported to preferentially form at carbide/ferrite interfaces [46,51,52], approximating the carbide shapes and aspect ratios by omnidirectional dissolution. The resultant retained austenite shells surrounding residual carbides in the form of core-shell particles observed in this work (Figs. 5a and 6b) were also reported by Miyamoto et al. [39] for manganese (Mn)–C steels around partially dissolved cementite. In their work, such retained austenite was excluded for Cr-alloyed steel, which the authors related to necessary Cr partitioning out of the growing austenite at the observed lower temperatures (800 °C). However, retained austenite had been found adjacent to $M_{23}C_6$ after rapid heating experiments at higher temperatures (1200 °C) [52], where negligible partitioning [53] was predicted [39]. The present results obtained under similar annealing conditions (Fig. 6a and c) clearly show a correlation of retained austenite with both, Cr and C enrichment, as well as the absence of discontinuous composition changes associated with partitioning [39].

The blended microstructure (Section 1) achieved by the presented vessel processing approach (Fig. 2a) led to ultra-high strength at noticeable ductility (Fig. 7). Reference processing without prior accumulation of Cr and C resulted in a similar non-tempered martensitic matrix, showing no plastic deformation at comparable hardness in the absence of austenite. Apparently, the ultra-high-strength non-tempered martensitic matrix could be deformed under tensile loads through the incorporation of finely dispersed ductile retained austenite following the presented processing approach. The mechanical properties exhibited by this dispersed vessel microstructure can be tuned further by changing the austenite fraction and blended properties via different dissolution parameters (Section 4.3). However, dissolution at lower temperatures (1100 °C) seems to produce a more ductile material despite lower austenite fractions, while more complete dissolution at the highest temperatures (1300 °C) appears to produce a brittle phase mixture, even when including the highest austenite fraction (Table 1). These results point at a complex interdependence of carbide dissolution with the retained austenite fraction, the austenite's mechanical stabil-

ity and compliance and the hardness of the matrix. Future work will aim at investigating the effect of different processing parameters, as well as austenite morphologies (Fig. 8) and volume fractions on the mechanical properties, as well as chemical variations for modifying the transformation behavior of the retained austenite.

5.2. Kinetics of the carbide dissolution

The transient heat treatment performed to dissolve the vessel carbides represents the most critical processing step of the presented approach. Only if a balance is established between the stability of the $M_{23}C_6$ particles and the diffusion kinetics of Cr and C being released into the matrix (re-approaching homogeneous bulk concentration values), will austenite be retained upon quenching due to the locally lowered M_S temperature. The investigated parameter window ranged from 850 to 1350 °C for the annealing temperature, in a timeframe of 1–90 s. As is known from time-temperature-austenitization diagrams, and in accordance with literature reports, shorter annealing times require higher temperatures to achieve the desired carbide dissolution [39,54,55]. In this work the maximum amount of retained austenite (14.1 vol.%) could be obtained by annealing at 1200 °C for 3 s, within a kinetic window closing with temperature (Table 1).

An efficient way to determine the processing window and to understand the underlying phenomena is to gauge gradient formation, as well as Cr and C fluxes, by DICTRA calculations. Actual processing can hence be simulated by relying on the assumption of local equilibrium at the moving interface [53], and unrestricted interface mobility [48]. The accumulated microstructure (Fig. 4a) was replicated by a spherical calculation cell, discretized by a linear grid, containing a single carbide under accumulation stage conditions (Fig. 2b) at its center, surrounded by ferrite. An austenite nucleus (set as “inactive phase”) was placed at the interface of ferrite and carbide. Within the carbide, diffusion cannot be treated (“diffusion-none phase”). The cell is subjected to experimental heating rates, driving carbide dissolution and growth of austenite. Effects of different nucleation sites, surface energy contributions and interface phenomena were not treated. The calculated phase volume fractions for the chosen representative cell are contrasted with measured retained austenite fractions (XRD data), after quenching from selected conditions, in Fig. 9a. The decrease in carbide volume fraction follows a sigmoid shape, related almost exclusively to increasing temperature, as opposed to matrix phase transformation (855 °C). The calculated rapid carbide dissolution is reflected by a concurrent increase in measured retained austenite fraction. The shift between calculated carbide dissolution and measured austenite retention kinetics may be explained by the variation in carbide sizes (Fig. 4a), as well as impingement and overlap of some of the gradient zones [56,57] not considered in the calculations. Alternatively, restricted interface mobility [27,57] and/or the heating rate strongly increasing the $M_{23}C_6$ dissolution temperature [58], may have led to an overestimation of kinetics.

Within certain limitations, DICTRA thus seems to provide a reasonable description of the dissolution kinetics, indicating a quite narrow processing window for persisting chemical gradients, as was observed experimentally. In

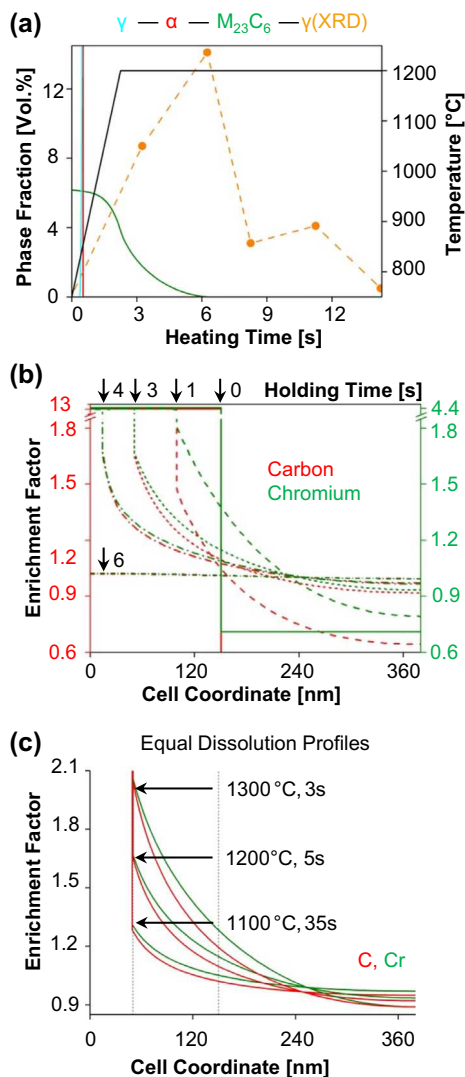


Fig. 9. DICTRA calculations of the carbide dissolution: (a) calculated phase fractions vs. temperature, together with retained austenite fraction measured by XRD; (b) enrichment factor gradients in Cr and C, calculated for selected holding times; (c) comparable dissolution states for different holding temperatures and heating times, chosen to each decrease the spherical carbide radius to 33%, from initially 150 nm.

Fig. 9b the enrichment factors for Cr and C, i.e. the ratio of the local to the bulk composition values [48], are plotted against the cell coordinate. For reference, spot measurements of austenite by Auger and TEM EDS gave Cr enrichment factors of 1.8 and 1.9, respectively. As carbide dissolution is negligible during the beginning of heating (Fig. 9a), especially within the ferrite regime [46], the calculated gradients are shown only for (selected) holding times at 1200 °C (Fig. 9b). The boundary condition at the moving carbide–austenite interface is controlled by the mass balance and the chemical potentials which vary with time and temperature. Hence, the Cr and C enrichment-factor gradients quickly converge in slope and magnitude after reaching the holding temperature. C enrichment is initially lower, owing to dissolution in the ferrite regime. The experimentally quantified Cr enrichment levels (1.8, 1.9; Section 4.2) are barely reached by the calculation, implying slightly higher actual elemental pile-ups in the microstructure.

Transferring the calculated enrichment gradients to the Schaeffler diagram (Fig. 2d) allows us to gauge whether retained austenite can be expected on quenching in the calculated case. Thus, in the event of quenching during dissolution, a shell of retained austenite is indeed predicted to remain around the carbide. Traces of attendant delta ferrite, previously observed under similar conditions [52], might also occur during the early dissolution stages of regions with high Cr enrichment (Fig. 9b; 1 s). How fast the respective enrichment pile-ups, shown to stabilize austenite, can be dissipated, depends on their magnitude and the mobility of their constituents. In Fig. 9c gradients are shown, which were calculated for identical dissolution states while heating to and holding at 1100, 1200 and 1300 °C. These calculation results confirm the experimental observations (Table 1) [55,52]; namely that higher temperatures induce higher elemental pile-ups [59], but also lead to faster dissipation of gradients due to increased diffusivity, and thereby narrow the available kinetic window.

5.3. Transfer of the approach to other materials and alloy concepts

While the presented approach may be applied to any metallic alloy systems exhibiting the required thermodynamic characteristics (Section 1), it is most effectively employed on steels, due to the multitude of attainable phases, most of which are accessible through the transformation of austenite.

In any case, the type of vessel phase – determined by the alloy concept and precipitation parameters – allows us to choose which elements to accumulate for the desired microstructure build-up. Cr accumulations conceivably may also be used for locally stabilizing ferrite [60] in an austenitic matrix for a duplex microstructure, whereas C gradients could enable martensite islands at specific locations within ferrite to optimize the mechanical properties of DP steels. Furthermore, different vessel phases can be selected depending on their stability against dissolution to modify the processing window of this heat treatment step, or to change the location and morphology of the chemical gradients by different nucleation and growth regimes. Possible candidates for vessels are intermetallic phases of limited stability, such as the sigma [61] or chi phase [62], or various types of carbides such as M_3C -cementite [39], or Fe_3AlC κ -carbides [63]. M_7C_3 carbides were found to function as vessels in a way analogous to $M_{23}C_6$, but with lower Cr levels and thus lower stabilized austenite fractions. The presented Fe–Cr–C model alloy could be further optimized in terms of adapted processing such as additional tempering after dissolution, but potentially also by introducing other alloying elements. For instance, Mn [39] or molybdenum [64] may be added to change the diffusion kinetics of C, thus broadening the processing window for dissolution to longer annealing times, and to affect the stability of the retained austenite against transformation during deformation.

6. Summary and conclusions

In this study a new processing approach is presented to locally design multiphase structural materials. It is based on utilizing the growth and dissolution of vessel phases to obtain controlled chemical gradients within the microstructure. The vessel phase method includes the three steps of

matrix homogenization (conditioning step), vessel phase precipitation (accumulation step) and vessel dissolution (dissolution step). Variation of the thermomechanical parameters of the processing sequence allows for designing the local microstructure build-up and thus the mechanical properties of advanced structural materials. The approach was validated on the example of a 11.6Cr–0.32C (wt.%) steel, where $M_{23}C_6$ carbides were used to accumulate Cr and C to achieve various tailored blended austenitic/martensitic microstructures. The following conclusions can be drawn:

- (1) EPMA, EBSD, TEM and Auger measurements correlated the local enrichment of Cr and C with austenite retention at the former location of the dissolved carbide vessels, where the M_S temperature was consequently lowered. This concept of local enrichment and stabilization may be exploited for designing novel lean alloy compositions and microstructures with complex phases.
- (2) Austenite fractions of up to 14.1 vol.% could be obtained within a martensitic matrix. The processing window to obtain the required inhomogeneous austenite, i.e. annealing time and temperature for the vessels dissolution as the most critical processing step, requires balancing the stability of carbides and the diffusion kinetics of Cr and C into the matrix. Changes in alloying or processing may serve to optimize this kinetic window.
- (3) DICTRA calculations were shown to viably predict and evaluate carbide dissolution for transient heat treatment conditions by approximating microstructural conditions, thus testing and extending the range of experimental observation. In this way, austenite retention kinetics could be related to local mass balance and diffusion to guide processing.
- (4) As the location and morphology of the chemical gradients are inherited from the vessel phases, various austenite morphologies could be achieved by changing the parameters of the processing sequence (matrix conditioning, growth of the vessel phases, dissolution). In this way, multiple pathways can be opened for designing various multiphase microstructures of the desired local constitution, morphology and transformation behavior.
- (5) The fine dispersion of retained austenite obtained by the proposed processing step made the strong but brittle non-tempered martensitic matrix accessible to tensile loading, so that an ultimate tensile strength of 1900 MPa at ~8% elongation could be reached without sacrificing hardness. On this basis, additional tempering treatments may be applied to further tune the mechanical properties.

Acknowledgment

Erika Bartsch is gratefully acknowledged for TEM operation and diffraction analysis, as is Dr. Sergij Borodin for conducting Auger spectroscopy and evaluation.

References

- [1] R.O. Ritchie, *Nat. Mater.* 10 (2011) 817.
- [2] D. Raabe, D. Ponge, O. Dmitrieva, B. Sander, *Adv. Eng. Mater.* 11 (2009) 547.
- [3] I. Gutierrez-Urrutia, D. Raabe, *Acta Mater.* 60 (2012) 5791.
- [4] M. Calcagnotto, D. Ponge, D. Raabe, *Mater. Sci. Eng., A* 527 (2010) 7832.
- [5] Z. Jiang, Z. Guan, J. Lian, *Mater. Sci. Eng., A* 190 (1995) 55.
- [6] G.R. Speich, V.A. Demarest, R.L. Miller, *Metall. Trans. A* 12A (1981) 1419.
- [7] Y.S. Zheng, Z.G. Wang, S.H. Ai, *Mater. Sci. Eng., A* 176 (1994) 393.
- [8] T. Lolla, G. Cola, B. Narayanan, B. Alexandrov, S.S. Babu, *Mater. Sci. Technol.* 27 (2011) 863.
- [9] C. Garcia-Mateo, F.G. Cabellero, H.K.D.H. Badeshia, *ISIJ Int.* 43 (2003) 1238.
- [10] H. Springer, M. Belde, D. Raabe, *Mater. Sci. Eng.* 582 (2013) 235.
- [11] L. Yuan, D. Ponge, J. Wittig, P. Choi, J.A. Jiménez, D. Raabe, *Acta Mater.* 60 (2012) 2790.
- [12] G.B. Olson, M. Cohen, *J. Less Common Metals* 28 (1972) 107.
- [13] J. Wang, S. van der Zwaag, *Metall. Mater. Trans. A* 32A (2001) 1527.
- [14] J.C. Lippold, J.D. Kotecki, *Welding Metallurgy and Weldability of Stainless Steel*, Wiley, Hoboken, NJ, 2005.
- [15] A.L. Schaeffler, *The Iron Age* (1948) 72.
- [16] E. De Moor, D.K. Matlock, J.G. Speer, M.J. Merwin, *Scripta Mater.* 64 (2011) 185.
- [17] N.C. Goel, J.P. Chakravarty, K. Tangri, *Metall. Trans. A* 18 (1987) 5.
- [18] J. Speer, D.K. Matlock, B.C. De Cooman, J.G. Schroth, *Acta Mater.* 51 (2003) 2611.
- [19] J. Wang, S. van der Zwaag, *Metall. Mater. Trans.* 32A (2001) 1527.
- [20] D. Raabe, S. Sandlöbes, J. Millán, D. Ponge, H. Assadi, M. Herbig, et al., *Acta Mater.* 61 (2013) 6132.
- [21] K. Zhang, M. Zhang, Z. Guo, N. Chen, Y. Rong, *Mater. Sci. Eng.* 528 (2011) 8486.
- [22] T. Tsuchiyama, J. Tobata, T. Tao, N. Nakada, S. Takaki, *Mater. Sci. Eng., A* 532 (2012) 585.
- [23] E. De Moor, S. Lacroix, L. Samek, J. Penning, J.G. Speer, in: *The 3rd International Conference on Advanced Structural Steels*, Gyeongju, Korea, 2006.
- [24] N.J. Kim, G. Thomas, *Metall. Trans. A* 12A (1981) 483.
- [25] D.Q. Bai, A.D. Chiro, S. Yue, *Mater. Sci. Forum* 284 (1998) 253.
- [26] G.N. Haidemenopoulos, A.N. Vasilakos, *Steel Res.* 67 11 (1996) 513.
- [27] G. Molinder, *Acta Metall.* 4 (1956) 565.
- [28] L. Kaufman, H. Bernstein, *Computer Calculations of Phase Diagrams*, Academic Press, New York, 1970.
- [29] N. Saunders, A.P. Miodownik, in: R.W. Cahn (Ed.), *Calphad Calculations of Phase Diagrams*, A Comprehensive Guide, Pergamon Materials Series, Pergamon Press, Elmsford, NJ, 1998.
- [30] W. Song, J. von Appen, P. Choi, R. Dronskowski, D. Raabe, W. Bleck, *Acta Mater.* 61 (2013) 7582.
- [31] W. Song, P.P. Choi, G. Inden, W. Song, U. Prah, D. Raabe, W. Bleck, *Tran. Phys. Metall. Mater. Sci.* 45A (2014) 595.
- [32] J. Bratberg, K. Frisk, *Metall. Mater. Trans. A* 35A (2004) 3649.
- [33] G. Miyamoto, J.C. Oh, K. Hono, T. Furuhashi, T. Maki, *Acta Mater.* 55 (2007) 5027.
- [34] J.V. Bee, P.R. Howell, R.W.K. Honeycombe, *Metall. Trans. A* 10A (1979) 1207.
- [35] M. Hillert, K. Nilsson, L.-E. Törndahl, *J. Iron Steel Inst.* (1971) 49.
- [36] M. Taneike, K. Sawada, F. Abe, *Metall. Mater. Trans. A* 35A (2004) 1255.
- [37] Å. Gustafson, M. Hättestrand, *Mater. Sci. Eng., A* A333 (2002) 279.
- [38] H. Finkler, M. Schirra, *Steel Res.* 67 67 (1996) 328.
- [39] G. Miyamoto, H. Usuki, Z.-D. Li, T. Furuhashi, *Acta Mater.* 58 (2010) 4492.
- [40] M.R. Plichta, H.I. Aaronson, *Metall. Trans.* 5 (1974) 2611.

- [41] J.O. Andersson, T. Helander, L. Höglund, P.F. Shi, B. Sundman, *Calphad* 26 (2002) 273.
- [42] L. Lutterotti, S. Matthies, H.R. Wenk, MAUD (Material Analysis Using Diffraction): a user friendly Java program for Rietveld texture analysis and more, in: *Proceeding of the Twelfth International Conference on Textures of Materials (ICOTOM-12)*, vol. 1, 1999, p. 1599.
- [43] D.V. Shtansky, K. Nakai, Y. Ohmori, *Acta Mater.* 48 (2000) 969.
- [44] M.D. Abramoff, P.J. Magalhaes, S.J. Ram, *Image processing with ImageJ*, *Biophotonics Int.* 11–7 (2004) 36.
- [45] D. Briggs, M.P. Seah, *Practical Surface Analysis: Auger and X-ray Photoelectron Spectroscopy*, Wiley, New York, 1990.
- [46] P.R. Judd, H.W. Paxton, *Trans. Metall. Soc. AIME* 242 (1968) 206.
- [47] F. Abe, *Sci. Technol. Adv. Mater.* 9 (2008) 1.
- [48] O. Dmitrieva, D. Ponge, G. Inden, J. Millán, P. Choi, J. Sietsma, D. Raabe, *Acta Mater.* 59 (2011) 364.
- [49] D.R. Barraclough, D.J. Gooch, *Mater. Sci. Technol.* 1 (1985) 961.
- [50] R.A. Grange, *Metall. Trans.* 2 (1971) 65.
- [51] T. Furuhashi, K. Kikumoto, H. Saito, T. Sekine, T. Ogawa, S. Morito, T. Maki, *ISIJ Int.* 48–8 (2008) 1038.
- [52] D.V. Shtansky, K. Nakai, Y. Ohmori, *Acta Mater.* 48 (2000) 1679.
- [53] M. Hillert, *Internat Rep.*, Swedish Inst. Metal Res., 1953.
- [54] J. Epp, H. Surm, O. Kessler, T. Hirsch, *Acta Mater.* 55 (2007) 5959.
- [55] J. Orlich, H.J. Pietrzeniuk, *Atlas zur Wärmebehandlung der Stähle*, Bd. 4, 2. Teil, Düsseldorf: Stahleisen, 1976.
- [56] G. Wang, D.S. Xu, N. Ma, N. Zhou, E.J. Payton, R. Yang, M.J. Mills, Y. Wang, *Acta Mater.* 57 (2009) 316.
- [57] Z.Q. Liu, G. Miyamoto, Z.G. Yang, T. Furuhashi, *Acta Mater.* 61 (2013) 3120.
- [58] C.G. de Andres, G. Caruana, L.F. Alvarez, *Mater. Sci. Eng. A241* (1998) 211.
- [59] M. Hillert, L. Höglund, Ågren J. *Acta Metall. Mater.* 41–7 (1993) 1951.
- [60] D.V. Shtansky, K. Nakai, Y. Ohmori, *Z. Metallkd.* 90 (1) (1999) 25.
- [61] C.C. Hsieh, D. Lin, W. Wu, *Met. Mater. Int.* 13–5 (2012) 359.
- [62] J. Dobranszky, P.J. Szabo, T. Berecz, V. Hrotko, M. Portko, *Spectrochim. Acta Part B B59* (2004) 1781.
- [63] Y. Kimura, K. Handa, K. Hayashi, Y. Mishima, *Intermetallics* 12 (2004) 607.
- [64] K.R. Kinsman, H.I. Aaronson, *Transformation and Hardenability in Steels*, Climax Molybdenum Co., Ann Arbor, MI, 1967, p. 39.